

Effects of High-Frequency Damping on Iterative Convergence of Implicit Viscous Solver

Hiroaki Nishikawa*

National Institute of Aerospace, Hampton, VA 23666, USA

Yoshitaka Nakashima and Norihiko Watanabe†

Software Cradle Co., Ltd, Osaka, JAPAN

July 22, 2017

Abstract

This paper discusses effects of high-frequency damping on iterative convergence of an implicit defect-correction solver for viscous problems. The study targets a finite-volume discretization with a one parameter family of damped viscous schemes. The parameter α controls high-frequency damping: zero damping with $\alpha = 0$, and larger damping for larger $\alpha (> 0)$. Convergence rates are predicted for a model diffusion equation by a Fourier analysis over a practical range of α . It is shown that the convergence rate attains its minimum at $\alpha = 1$ on regular quadrilateral grids, and deteriorates for larger values of α . A similar behavior is observed for regular triangular grids. In both quadrilateral and triangular grids, the solver is predicted to diverge for α smaller than approximately 0.5. Numerical results are shown for the diffusion equation and the Navier-Stokes equations on regular and irregular grids. The study suggests that $\alpha = 1$ and $4/3$ are suitable values for robust and efficient computations, and $\alpha = 4/3$ is recommended for the diffusion equation, which achieves higher-order accuracy on regular quadrilateral grids. Finally, a Jacobian-Free Newton-Krylov solver with the implicit solver (a low-order Jacobian approximately inverted by a multi-color Gauss-Seidel relaxation scheme) used as a variable preconditioner is recommended for practical computations, which provides robust and efficient convergence for a wide range of α .

1 Introduction

Computational Fluid Dynamics (CFD) simulations have been widely used in industrial applications, but unstructured-grid technologies for practical complex geometries still require improved robustness and efficiency to meet the ever-increasing demand for accurate and efficient high-fidelity simulations. Improvements are sought in grid adaptation, solver constructions, and high-performance computing. More fundamentally, improvements in viscous discretizations have also been recognized as important especially on unstructured grids, not only for accuracy, but also for robust and efficient solver constructions. For example, improved viscous discretizations have been found to dramatically improve the performance of iterative solvers [1, 2].

In the recent works [3, 4, 5], two essential components have been emphasized for robust and accurate viscous discretizations: consistent and damping terms. The consistent term approximates viscous terms consistently: it approaches the exact viscous terms in the grid refinement. The damping term, on the other hand, does not approximate the viscous terms (i.e., it vanishes in the grid refinement), but provides a high-frequency damping property, which has been found critically important for robust and accurate computations on unstructured grids. In many finite-volume viscous discretizations, however, these two mechanisms are not clearly identified. Thus, if a scheme fails, e.g., due to convergence difficulties or numerical oscillations, one typically attempts to devise a new scheme (e.g., Refs.[2, 6, 7]) or resort to a more robust but inconsistent scheme (e.g., Ref.[8]) although the problem may be resolved by increasing high-frequency damping hidden in the original scheme. See Ref.[3] (Appendix C) for damping terms identified for the so-called edge-normal and face-tangent diffusion schemes [2], and see also Ref.[9] for a damping term identified for a finite-difference-type scheme on unstructured grids proposed by Muppidi and Mahesh [10].

*Corresponding author.

†Currently, Associate Professor of Department of Mechanical Engineering at Sojo University, Japan.

In Ref.[4], diffusion schemes with adjustable damping terms have been derived for various discretization methods based on a general principle: extract a diffusion scheme from an upwind discretization of a hyperbolic diffusion system. Its general applicability has been demonstrated for various methods: finite-volume, residual-distribution, discontinuous Galerkin, and spectral-volume methods [4]. Extensions to high-order residual-distribution schemes for the Navier-Stokes equations can be found in Ref.[11]. The diffusion scheme derived for finite-volume methods, called the alpha-damping scheme, is similar to some existing schemes [12, 13], but has features not seen typically in other schemes. First, it directly incorporates a grid-skewness measure into the scheme, which has been found essential for accurate computations on highly-skewed unstructured viscous grids. Second, it has a non-dimensional parameter α that controls the amount of high-frequency damping. The parameter α acts on a solution jump at a cell interface, and therefore can be adjusted without affecting the consistency and the order of accuracy of the scheme (see analyses in Ref.[4]). Ref.[4] has shown that the damping parameter has also a significant impact on accuracy. For example, a second-order finite-volume diffusion scheme can potentially achieve fourth-order accuracy on Cartesian grids with $\alpha = 4/3$. Similarly, P_1 discontinuous-Galerkin and spectral-volume diffusion schemes achieve fourth-order accuracy with $\alpha = 6$ and $\alpha = 3$, respectively, on uniform grids [4]. The finite-volume scheme with $\alpha = 4/3$ has been shown to yield accurate solutions also on highly-skewed irregular anisotropic grids [4, 14] even though fourth-order accuracy cannot be obtained on such grids by $\alpha = 4/3$. The damping term of this kind also plays a key role in implementing weak boundary conditions [15, 16].

The alpha-damping scheme has been successfully used in a three-dimensional general-purpose unstructured-grid code in combination with an implicit solver, and demonstrated its robustness and efficiency on highly-stretched unstructured grids used in practical viscous simulations [17]. It is also employed in an improved finite-volume method for diffusion [18] and a high-order finite-volume method for RANS simulations [19]. A compact Jacobian matrix can be constructed for the implicit solver by the derivative of the damping term, which is similar to the derivative of the edge-terms-only (or a thin-layer approximation) scheme [2]. The skewness measure and the damping parameter α in the damping term are expected to play a critical role for an improved diagonal dominance on highly-skewed grids. However, effects of α on iterative convergence have not received much attention and were not well understood; although it has been known experimentally that the iterative convergence of an implicit solver deteriorates as α departs far from 1.0. Refs.[3, 4, 5] consider only explicit time-stepping schemes and solvers, and do not discuss implicit solvers. The objective of the present work is, therefore, to analyze the implicit iterative solver for the alpha-damping scheme, and provide a guide for choosing the parameter α for practical viscous computations. It is also shown that a robust and efficient Jacobian-Free Newton-Krylov solver can be developed with the implicit solver used as a variable preconditioner, which can converge for α with which the implicit solver diverges.

The target discretization is taken to be a node-centered edge-based discretization, but results are equally applicable to other finite-volume methods, e.g., cell-centered methods. The target solver is an implicit defect-correction solver with a compact Jacobian based on the derivative of the damping term only. A Fourier analysis is performed to predict the convergence rate of the implicit solver on regular quadrilateral and triangular grids for the diffusion (Laplace) operator, modeling the viscous term in the incompressible Navier-Stokes equations. For regular quadrilateral grids, the analysis shows that the convergence rate is zero at $\alpha = 1.0$, increases towards 1.0 for α larger and smaller than 1.0, and exceeds 1.0 for $\alpha \leq 0.5$. A similar behavior is observed for regular triangular grids. Numerical results are shown for diffusion on regular grids to confirm the predicted behaviors of the implicit solver, and also on irregular grids to examine how the convergence is affected by mesh irregularities. Besides the impact of alpha on the convergence rate, we also address its impact on accuracy. To provide implications on compressible viscous flow solvers, numerical results are shown for two-dimensional compressible Navier-Stokes equations.

The paper is organized as follows. In Section 2, target discretization and implicit solvers are described. In Section 3, a Fourier analysis is performed for regular grids and the convergence rate of an implicit iterative solver is determined. In Section 4, numerical results are presented to confirm the convergence behavior predicted by the analysis, and to investigate the performance of implicit solvers for more general cases, including irregular grids and viscous flow simulations. Finally, Section 5 concludes the paper with remarks.

2 Target Discretization and Solver

2.1 Target Discretization: Edge-Based (Finite-Volume) Method

Consider the diffusion equation (the Poisson equation), which models the viscous term in incompressible flows:

$$\partial_{xx}u + \partial_{yy}u = f, \quad (2.1)$$

where u is a solution variable and $f = f(x, y)$ is a forcing term. To discretize it on unstructured grids, we consider the node-centered edge-based discretization [17, 20, 21, 22, 23, 24, 25, 26]. The residual equation at a node j is given by

$$Res_j = \sum_{k \in \{k_j\}} \phi_{jk} A_{jk} - f_j V_j = 0, \quad (2.2)$$

where V_j is the measure of the dual control volume around the node j , $\{k_j\}$ is a set of neighbors of the node j , ϕ_{jk} is a numerical flux defined at the edge midpoint, and A_{jk} is the magnitude of the directed area vector $\mathbf{n}_{jk} = A_{jk} \hat{\mathbf{n}}_{jk}$. See Figures 1 for a triangular grid and 2 for a quadrilateral grid. In this study, we focus on arbitrary triangular grids and orthogonal quadrilateral grids. For second-order accuracy, the linear reconstruction employs the solution gradient computed from the solution values. On regular quadrilateral and triangular grids, the gradients can be computed by the central difference formula at interior nodes, and a one-sided second-order finite-difference formula or a quadratic least-squares (LSQ) fit at boundary nodes. The second-order formulas are necessary to achieve higher-order accuracy for a special value of α on regular quadrilateral grids as mentioned below. For irregular triangular grids, since there are no special values of α , a linear LSQ fit is employed to compute the gradients. The alpha-damping scheme is defined by the following numerical flux:

$$\phi_{jk} = \frac{\nu}{2} [(\nabla u)_j + (\nabla u)_k] \cdot \hat{\mathbf{n}}_{jk} + \frac{\nu\alpha}{2L_r} (u_R - u_L), \quad (2.3)$$

where $(\nabla u)_j$ and $(\nabla u)_k$ are the gradients at the nodes j and k , respectively, $\hat{\mathbf{n}}_{jk}$ is the unit directed area vector, u_L and u_R are linearly reconstructed solutions at the edge-midpoint,

$$u_L = u_j + \frac{1}{2}(\nabla u)_j \cdot \mathbf{e}_{jk}, \quad u_R = u_k - \frac{1}{2}(\nabla u)_k \cdot \mathbf{e}_{jk}, \quad \mathbf{e}_{jk} = (x_k - x_j, y_k - y_j), \quad (2.4)$$

and L_r is the length scale, which incorporates the skewness measure $\hat{\mathbf{e}}_{jk} \cdot \hat{\mathbf{n}}_{jk}$, where $\hat{\mathbf{e}}_{jk} = \mathbf{e}_{jk}/|\mathbf{e}_{jk}|$ (see Figure 3),

$$L_r = \frac{1}{2} |\mathbf{e}_{jk} \cdot \hat{\mathbf{n}}_{jk}|. \quad (2.5)$$

The first term in the numerical flux (2.3) represents the averaged gradients; this is the consistent term that approximates the true diffusive flux. The second term is the damping term, which does not approximate the diffusive flux, but provides high-frequency damping [4]. It is important to note that the consistent term approaches the physical flux and the damping term approaches zero in the grid refinement. The damping term is a high-order term similar to the dissipation term in the upwind flux for second-order advection schemes, solely responsible for high-frequency damping. The parameter α is the coefficient that controls the damping: zero damping with $\alpha = 0$, and larger damping for larger $\alpha (> 0)$ as shown by a Fourier analysis in Ref.[4] (see Figure 4.2 in Ref.[4]). Note that the parameter can take any non-negative value without losing the consistency of the scheme since the damping term has the order property of vanishing in the grid refinement. It is known that $\alpha = 4/3$ gives fourth-order accuracy on regular quadrilateral grids as demonstrated for a cell-centered method in Ref.[4]. For the node-centered edge-based scheme considered in this work, however, third-order order accuracy is observed. Fourth-order accuracy with $\alpha = 4/3$ is achieved by a special error cancellation on a regular stencil at interior nodes [4], and it is lost at nodes connected to boundary nodes because of an irregular stencil used to compute the gradient at the boundary nodes. In Ref.[4], a cell-centered finite-volume method was used, for which fourth-order accuracy can be obtained with the use of a ghost cell.

Note that the edge-based discretization is equivalent to a cell-centered finite-volume discretization formulated on a dual polyhedral grid. On Cartesian grids, it is equivalent to a cell-centered finite-volume or a finite-difference

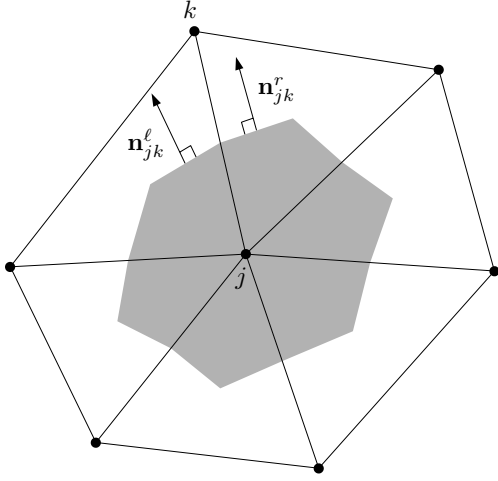


Figure 1: Triangular stencil and face normals that define the directed area vector: $\mathbf{n}_{jk} = \mathbf{n}_{jk}^l + \mathbf{n}_{jk}^r$.

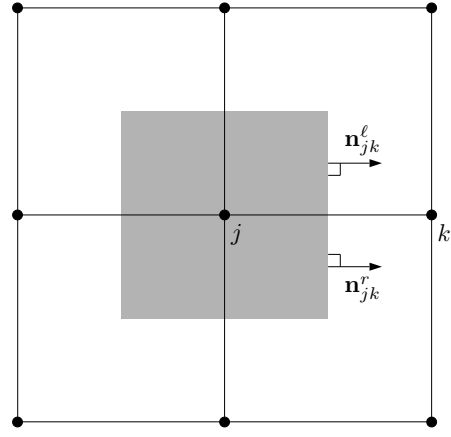


Figure 2: Quadrilateral stencil and face normals that define the directed area vector: $\mathbf{n}_{jk} = \mathbf{n}_{jk}^l + \mathbf{n}_{jk}^r$.

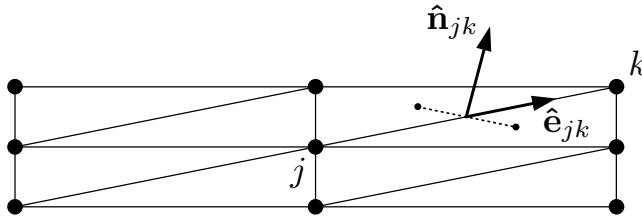


Figure 3: Vectors that define the skewness measure $\hat{\mathbf{e}}_{jk} \cdot \hat{\mathbf{n}}_{jk}$. The hat indicates a unit vector.

scheme, at least, away from boundaries. Therefore, the analysis presented below should provide useful indications to these schemes. It is also important to note that the alpha-damping diffusion flux (2.3) can be expressed as

$$\phi_{jk} = \nu (\overline{\nabla u}) \cdot \hat{\mathbf{n}}_{jk}, \quad \overline{\nabla u} = \frac{1}{2} [(\nabla u)_j + (\nabla u)_k] + \frac{\alpha}{2L_r} (u_R - u_L) \hat{\mathbf{n}}_{jk}, \quad (2.6)$$

thus suggesting a gradient formula at the face. Hence, it can be immediately applied to the compressible Navier-Stokes equations: use the damped gradient $\overline{\nabla u}$ to evaluate the density, velocity, and temperature (or pressure) gradients at the control-volume face. In this work, we consider this simple approach for the compressible Navier-Stokes equations. See Ref.[5] for more details and an alternative approach to extending the alpha-damping scheme to the viscous terms.

2.2 Target Solver: Implicit Defect-Correction Solver

The discretized equations (2.2) are solved by an implicit defect-correction solver:

$$\mathbf{U}^{n+1} = \mathbf{U}^n + \Delta \mathbf{U}, \quad (2.7)$$

$$\frac{\partial \overline{\mathbf{Res}}}{\partial \mathbf{U}} \Delta \mathbf{U} = -\mathbf{Res}(\mathbf{U}^n), \quad (2.8)$$

where \mathbf{U} is a global vector of nodal solutions, \mathbf{Res} is a global vector of nodal residuals, and $\overline{\mathbf{Res}}$ is a global vector of lower-order residuals, which are defined by the low-order damping-term-only flux:

$$\phi_{jk} = \frac{\nu \alpha}{2L_r} (u_k - u_j). \quad (2.9)$$

The diagonal and off-diagonal elements in the j -th row are given by

$$\frac{\partial \overline{\text{Res}}_j}{\partial u_j} = - \sum_{k \in \{k_j\}} \frac{\nu \alpha}{2L_r} A_{jk}, \quad \frac{\partial \overline{\text{Res}}_j}{\partial u_k} = \frac{\nu \alpha}{2L_r} A_{jk}. \quad (2.10)$$

Therefore, the Jacobian is compact, depending only on the neighbors. For the compressible Navier-Stokes equations, the same approach has been taken, but the viscosity is not a constant and so the Jacobian involves the derivative of the viscosity; see Ref.[27] for details on the derivative of the viscous flux. Note that the damping-term-only flux, if used in the residual, leads to an inconsistent diffusion scheme on non-orthogonal grids [28, 29]. In the case of the compressible Navier-Stokes equations, it is known as the thin-layer approximation [2], which is an inconsistent scheme on any grid because shear components of the viscous stresses are totally ignored. However, the damping-term-only scheme is compact and robust with positive coefficients and thus can serve as a useful scheme for the construction of the Jacobian. In this paper, we analyze the convergence of the implicit defect-correction solver in relation to the parameter α for the model diffusion equation. In the analysis, we assume that the linear system is fully solved, but it is relaxed by a multi-color Gauss-Seidel method to a very low tolerance in actual numerical experiments.

As we will show, the implicit solver can diverge for a certain range of α . To secure robustness for practical applications, we consider a Jacobian-Free Newton-Krylov (JFNK) solver based the Generalized Conjugate Residual (GCR) method [30] with the above implicit defect-correction solver employed as a variable preconditioner [31, 32, 33]. More specifically, the damping-term-only Jacobian is used as a preconditioning matrix for the JFNK solver, and it is approximately inverted by the multi-color Gauss-Seidel relaxation scheme. In this method, we employ the GCR method to solve the linearized equation:

$$\frac{\partial \mathbf{Res}}{\partial \mathbf{U}} \Delta \mathbf{U} = -\mathbf{Res}(\mathbf{U}^n), \quad (2.11)$$

evaluated, without forming the exact Jacobian, as

$$\frac{\mathbf{Res}(\mathbf{U}^n + \epsilon \Delta \mathbf{U}) - \mathbf{Res}(\mathbf{U}^n)}{\epsilon} = -\mathbf{Res}(\mathbf{U}^n), \quad (2.12)$$

where ϵ is a small parameter as defined in Ref.[34]. The GCR projection is performed to reduce the residual of the above equation by one order of magnitude or for a specified maximum number of projections, and then the solution is updated as

$$\mathbf{U}^{n+1} = \mathbf{U}^n + \Delta \mathbf{U}. \quad (2.13)$$

The JFNK solver has the ability to converge even when the preconditioner diverges, which is well known and will be demonstrated later in the numerical experiments. This is because the multi-color Gauss-Seidel relaxation scheme is used only for preconditioning with a relatively large tolerance, typically one order magnitude reduction in the linear-system residual, and the GCR method is guaranteed not to diverge (a monotone convergence property) [31]. As in Ref.[32], the JFNK solver may be employed with a small number of projections, e.g., 4 or smaller, which provides robust convergence with a minimal cost of storing the Krylov vectors for practical large-scale problems. Effects of the number of projections will be investigated numerically later for a two-dimensional viscous flow problem. In the rest of the paper, the above JFNK solver is referred to as the JFNK-GCR solver.

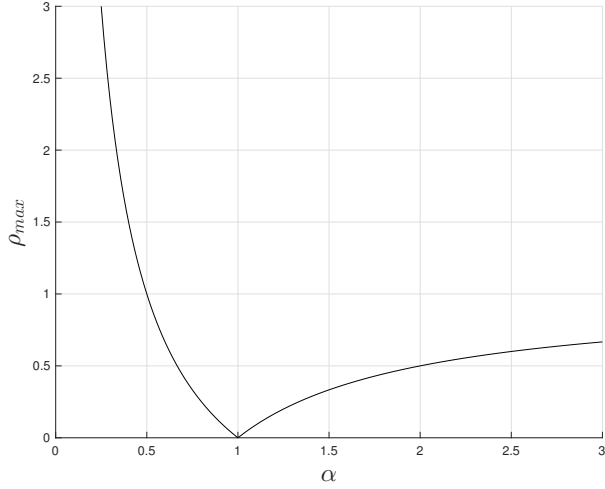
3 Analysis

3.1 Analysis Method

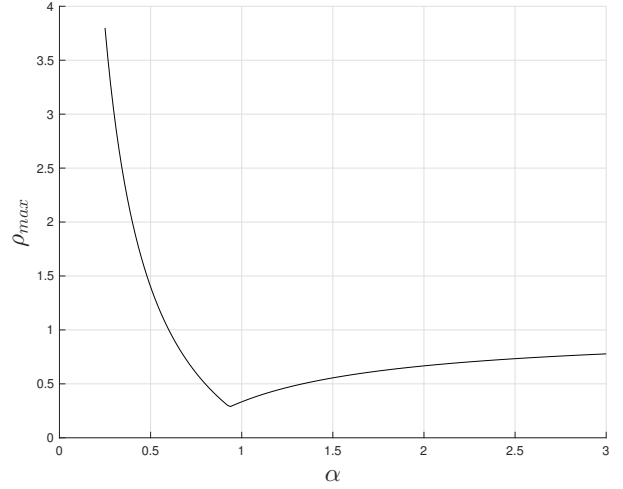
A Fourier analysis is performed for the implicit defect-correction solver on quadrilateral and triangular grids with uniform spacing in each coordinate direction. Boundary conditions are not taken into account, but the analysis provides indications of stability: e.g., if the convergence rate is greater than 1, the solver is expected to be unstable; a smaller convergence rate indicates a possibility of faster convergence [35, 36]. Numerical results will be presented later to demonstrate that the analysis accurately predicts the behavior of the solver.

Consider a Fourier mode

$$u^\beta = u_0^\beta \exp(\beta_x x/h_x + \beta_y y/h_y), \quad (3.1)$$



(a) Uniform quadrilateral grid.



(b) Uniform triangular grid.

Figure 4: Convergence rate versus the damping parameter α for an isotropic grid.

where u_0^β is the amplitude, β_x and β_y are frequencies (phase changes per grid spacing) in the x and y directions, respectively, and h_x and h_y are the corresponding grid spacings. Substituting the Fourier mode into Equation (2.7), we obtain

$$(u_0)^{n+1} = \rho(\beta_x, \beta_y) (u_0)^n, \quad \rho(\beta_x, \beta_y) = 1 - \frac{\lambda_R}{\lambda_J}, \quad (3.2)$$

where λ_R is the residual operator and λ_J is the Jacobian operator. The convergence rate of the implicit solver is determined by the maximum of $|\rho|$ taken over all frequencies:

$$\rho_{max} = \max_{\beta_x, \beta_y \in (-\pi, \pi)} |\rho(\beta_x, \beta_y)|. \quad (3.3)$$

The solver is stable if $\rho_{max} < 1$, converges faster for smaller ρ_{max} , and gets unstable if $\rho_{max} > 1$. The convergence rate will be evaluated for $\alpha = [0.25, 3]$ to investigate the effect of α on convergence.

3.2 Uniform Grid

For a regular quadrilateral grid as in Figure 6(a), we obtain

$$\rho(\beta_x, \beta_y) = \frac{(\alpha - 1) \{\cos(2\beta_x) + \cos(2\beta_y) - 2\}}{4\alpha \{\cos(\beta_x) + \cos(\beta_y) - 2\}}. \quad (3.4)$$

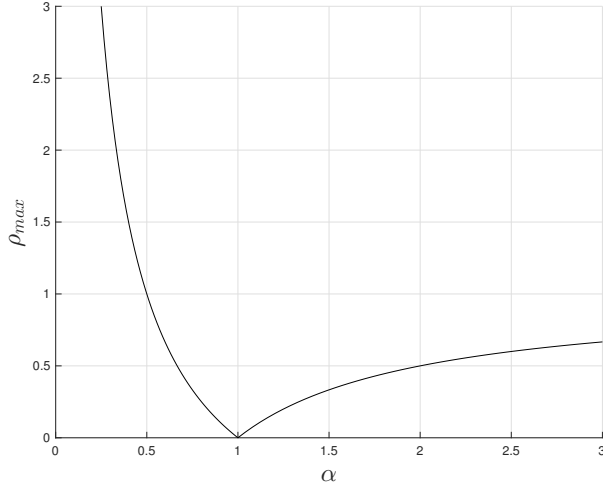
Observe that we have $\rho = 0$ for $\alpha = 1$, where the scheme reduces to the five-point central finite-difference scheme and the Jacobian becomes the exact linearization of the right hand side [4]. This is optimal for convergence, but not for accuracy since higher-order accuracy is achieved not for $\alpha = 1$ but for $\alpha = 4/3$. The convergence rate ρ_{max} was computed numerically as explained earlier, and the result is shown in Figure 4(a). First, it is observed that the convergence rate deteriorates as α increases from $\alpha = 1$. Therefore, as expected, the implicit solver converges faster for α closer to 1. Observe also that the solver diverges for $\alpha < 0.5$. A lack of damping leads to failure of the implicit solver.

For a regular triangular grid as illustrated in Figure 6(b), which is constructed by inserting diagonals into the quadrilateral grid, we obtain

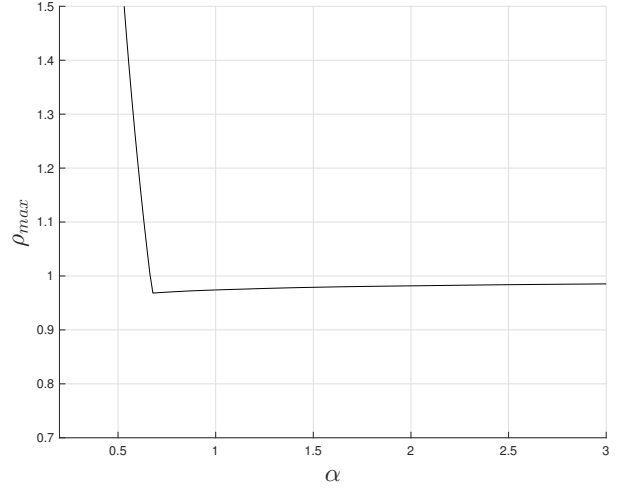
$$\rho(\beta_x, \beta_y) = \frac{X}{4\alpha \{5 \cos(\beta_x) + 5 \cos(\beta_y) + 2 \cos(\beta_x + \beta_y) - 12\}}, \quad (3.5)$$

where

$$\begin{aligned} X &= 2(\alpha - 1) \{\cos(\beta_x + 2\beta_y) + \cos(2\beta_x + \beta_y) - \cos(\beta_x) - \cos(\beta_y)\} \\ &\quad - 4 \{\cos(\beta_x - \beta_y) - \cos(\beta_x + \beta_y)\} + (5\alpha - 4) \{\cos(2\beta_x) + \cos(2\beta_y) - 2\}. \end{aligned} \quad (3.6)$$



(a) High-aspect-ratio quadrilateral grid.



(b) High-aspect-ratio triangular grid.

Figure 5: Convergence rate versus the damping parameter α for a high-aspect-ratio grid.

Figure 4(b) shows the convergence rate for the triangular grid. The minimum convergence rate is achieved not exactly at $\alpha = 1$, but the value slightly smaller than $\alpha = 1$. However, as in the quadrilateral-grid case, the convergence rate deteriorates for larger values. Also, the solver is predicted to diverge for α smaller than approximately 0.6.

Overall, the analysis suggests that $\alpha = 1$ is a reasonable choice. However, $\alpha = 4/3$ may be chosen for better accuracy at slightly slower convergence on quadrilateral grids.

3.3 High-Aspect-Ratio Grid

To investigate the effect of high aspect ratio cells, as typically required in high-Reynolds-number simulations, we consider a grid with uniform but different spacings in the two coordinate directions: h_x and h_y , in x and y directions, respectively. For a quadrilateral grid, we obtain

$$\begin{aligned} \rho(\beta_x, \beta_y) &= \frac{(\alpha - 1) \{h_y^2 \cos(2\beta_x) + h_x^2 \cos(2\beta_y) - h_x^2 - h_y^2\}}{4\alpha \{h_y^2 \cos(\beta_x) + h_x^2 \cos(\beta_y) - h_x^2 - h_y^2\}} \\ &= \frac{(\alpha - 1) \{\cos(2\beta_x) + R^2 \cos(2\beta_y) - R^2 - 1\}}{4\alpha \{\cos(\beta_x) + R^2 \cos(\beta_y) - R^2 - 1\}}, \end{aligned} \quad (3.7)$$

where $R = h_x/h_y$ is the aspect ratio. Figure 5(a) shows the convergence rate for $R = 10^3$. The result is very similar to the one for the isotropic grid, showing that the solver is not affected by the high aspect ratio on quadrilateral grids.

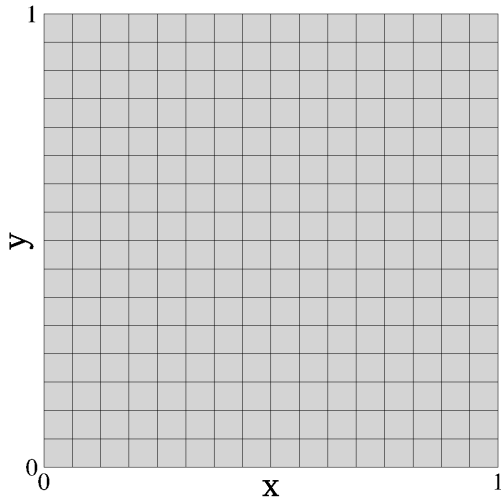
On the other hand, we obtain for a triangular grid

$$\rho(\beta_x, \beta_y) = \frac{X}{4\alpha \{(R^2 + 1) \cos(\beta_x + \beta_y) + (R^2 + 4) \cos(\beta_x) + (4R^2 + 1) \cos(\beta_y) - 6(R^2 + 1)\}}, \quad (3.8)$$

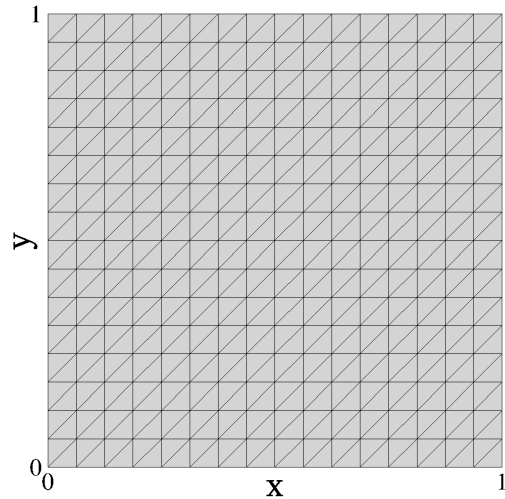
where

$$\begin{aligned} X &= (R^2\alpha + \alpha - 2R^2) \cos(\beta_x + 2\beta_y) + (R^2\alpha + \alpha - 2) \cos(2\beta_x + \beta_y) - (2R^2 + 2) \cos(\beta_x - \beta_y) \\ &+ (2R^2 + 2) \cos(\beta_x + \beta_y) + (R^2\alpha + 4\alpha - 4) \cos(2\beta_x) + (4R^2\alpha + \alpha - 4R^2) \cos(2\beta_y) \\ &- (R^2\alpha + \alpha - 2R^2) \cos(\beta_x) - (R^2\alpha + \alpha - 2) \cos(\beta_y) - (5\alpha - 4)(R^2 + 1), \end{aligned} \quad (3.9)$$

and the convergence rate computed for $R = 10^3$ is shown in Figure 5(b). The rate is still below 1.0 for a similar range as in the isotropic case, and thus stable, but much closer to 1.0, indicating slow down on high-aspect-ratio grids.

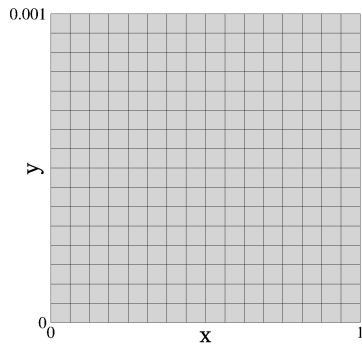


(a) 17×17 quadrilateral grid.

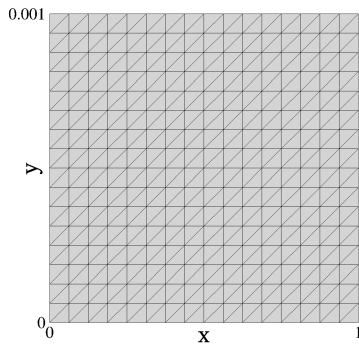


(b) 17×17 triangular grid.

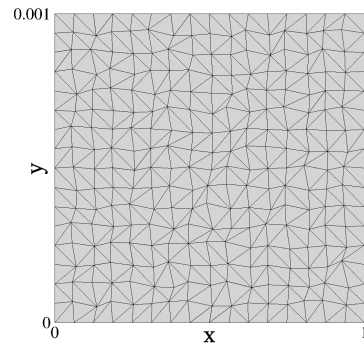
Figure 6: Uniform grids with $R = 1$.



(a) 17×17 quadrilateral grid.



(b) 17×17 triangular grid.



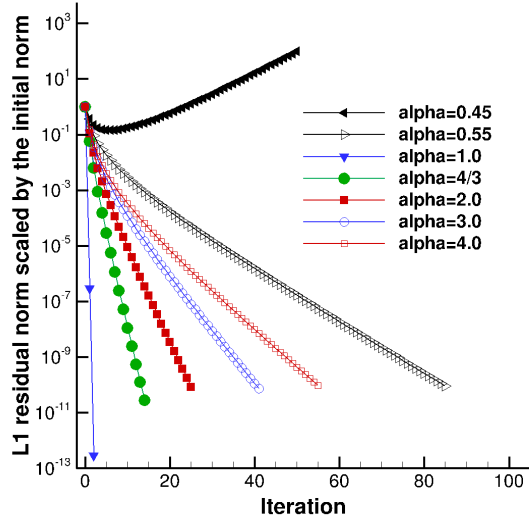
(c) 17×17 irregular triangular grid.

Figure 7: High-aspect-ratio grids with $R = 1000$.

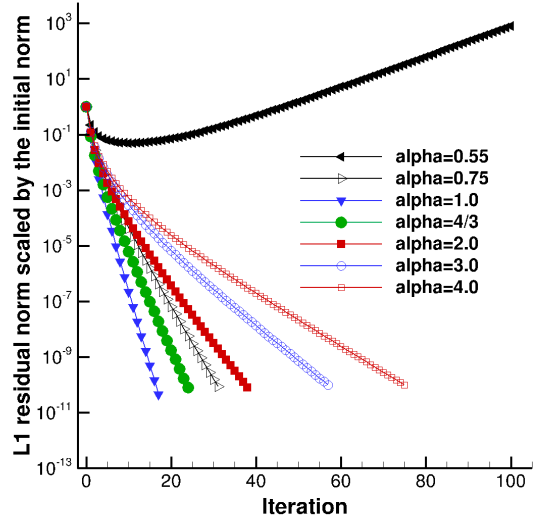
4 Numerical Results

4.1 Diffusion Equation

For all cases, the Dirichlet boundary condition is imposed strongly. To be consistent with the analysis, the linear system is sufficiently relaxed by the sequential Gauss-Seidel relaxation scheme until the linear residual is reduced by six orders of magnitude. The implicit solver is taken to be converged when the L_1 norm of the residual is reduced by ten orders of magnitude. For regular grids, the solution gradients are computed by the central-difference formula at interior nodes and an unweighted quadratic LSQ fit at boundary nodes. The LSQ fit uses neighbors of the neighbors to avoid ill-conditioning. For irregular grids, a linear LSQ fit is used. An initial solution is set by an exact solution with random perturbations. Three levels of grids with $n \times n$ nodes ($n = 17, 33, 65$) have been used for all grid types. The coarsest grids are shown in Figures 6 and 7: uniform quadrilateral grid (Figure 6(a)), uniform triangular grid (Figure 6(b)), high-aspect-ratio quadrilateral grid (Figure 7(a)), high-aspect-ratio triangular grid (Figure 7(b)), irregular high-aspect-ratio triangular grid (Figure 7(c)).

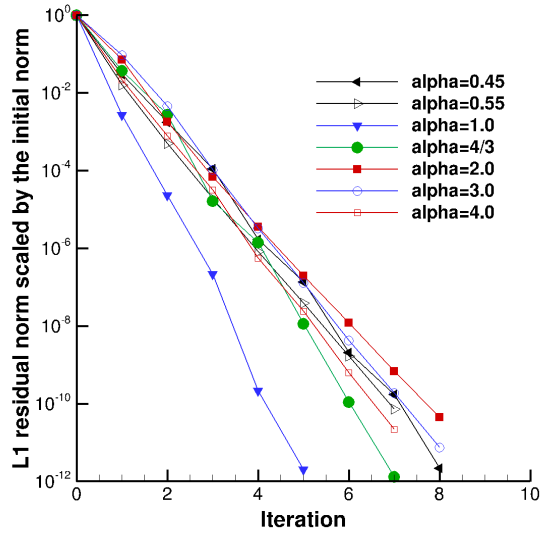


(a) 64×64 quadrilateral grid.

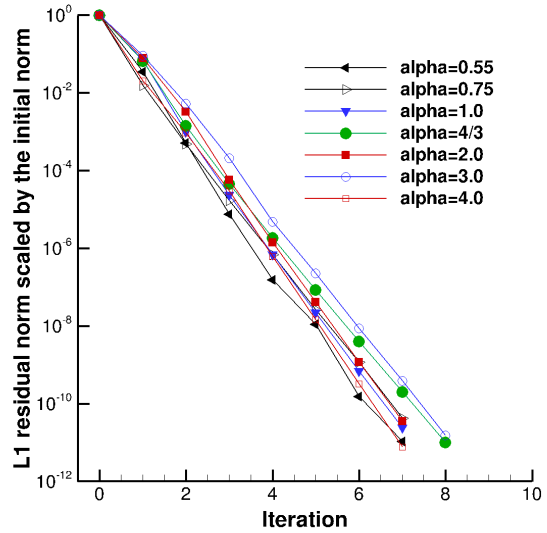


(b) 64×64 triangular grid.

Figure 8: Convergence histories of implicit defect-correction solver on a uniform grid with $R = 1$.



(a) 64×64 quadrilateral grid.



(b) 64×64 triangular grid.

Figure 9: Convergence histories of JFNK-GCR on a uniform grid with $R = 1$.

4.1.1 Uniform Grid

We consider the diffusion equation (2.1) with $f = 0$ in a square domain $(x, y) \in (0, 1) \times (0, 1)$. The exact solution is given by

$$u(x, y) = \frac{\sinh(\pi x) \sin(\pi y) + \sinh(\pi y) \sin(\pi x)}{\sinh(\pi)}. \quad (4.1)$$

Convergence results are shown for the 64×64 quadrilateral and triangular grids. Figure 8(a) shows the convergence histories for the quadrilateral-grid case. As predicted by the analysis, the convergence deteriorates as α increases from $\alpha = 1$ to $\alpha = 4$. The case $\alpha = 1$ shows a rapid convergence as expected; the solver becomes

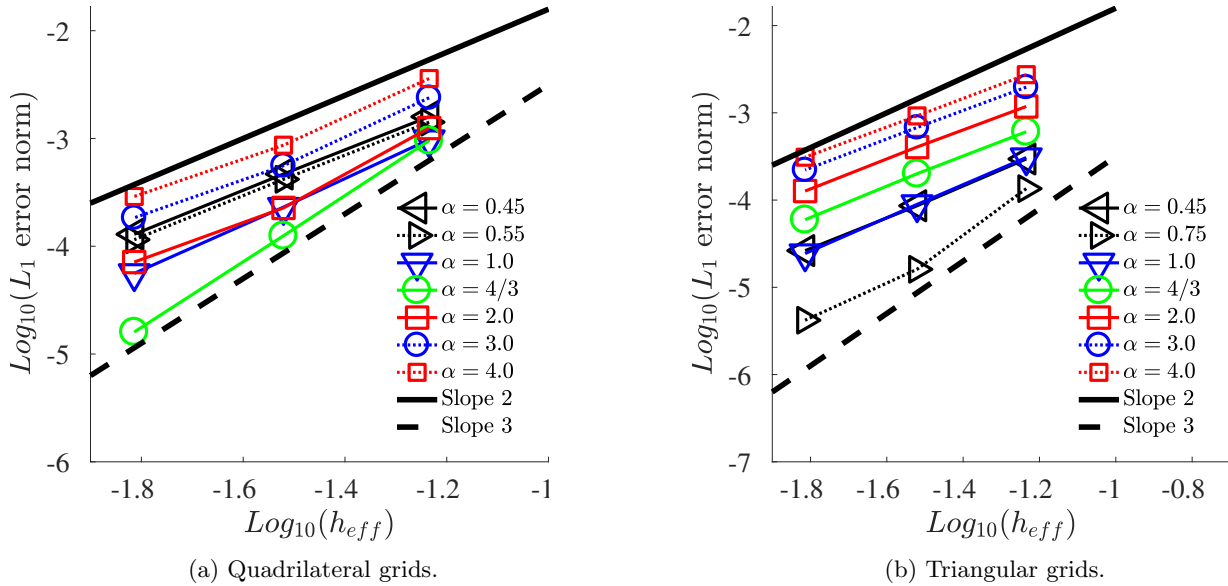


Figure 10: Error convergence for solutions obtained by the JFNK-GCR solver on uniform grids with $R = 1$.

Newton’s method in this case. Also, the solver converges for $\alpha = 0.55$ but diverges for $\alpha = 0.45$, which agrees with the analytical result: the solver diverges for $\alpha < 0.5$.

Similar results have been obtained for the triangular grid. See Figure 8(b). Again, as predicted by the analysis, the solver slows down for larger values of α . For the triangular grid, we considered cases $\alpha = 0.55$ and 0.75 , and found that the solver diverges $\alpha = 0.55$ but converges for 0.75 . It confirms the analytical prediction that the solver diverges when $\alpha < 0.6$, approximately.

It may be possible to stabilize the solver for small values of α by keeping $\alpha = 1$ in the residual Jacobian for any value of α in the residual. However, there is no strong reason to take $\alpha < 0.5$ since it would lead to a lack of damping and thus of robustness on general unstructured grids. A more practical strategy is to employ the JFNK-GCR solver, which has the ability to converge the residual even when the implicit solver (preconditioner) diverges. To demonstrate this, previous computations were repeated with the JFNK-GCR solver as described in Section 2.2. Results are shown in Figure 9. Clearly, the solver converges for all cases now, including those where the implicit solver diverges. Note that each iteration involves 10 preconditioner steps and residual evaluations to compute the Fréchet derivative (2.12). Therefore, the JFNK-GCR solver is not dramatically faster than the implicit solver.

Error convergence results are shown in Figure 10. The errors are plotted against the effective mesh spacing defined as the L_1 norm of the square root of control volumes around nodes. As shown in Figure 10(a), $\alpha = 4/3$ gives third-order accuracy while others yield second-order accuracy on uniform quadrilateral grids. Figure 10(b) shows the results for the triangular grids. The lowest error level is obtained with $\alpha = 0.75$, and the error increases for larger and smaller values of α . Note that no special values of α is theoretically known that achieves higher-order accuracy on triangular grids.

4.1.2 High-Aspect-Ratio Grid

We consider a domain $(x, y) \in (0, 1) \times (0, 0.001)$, and solve the diffusion equation (2.1) with

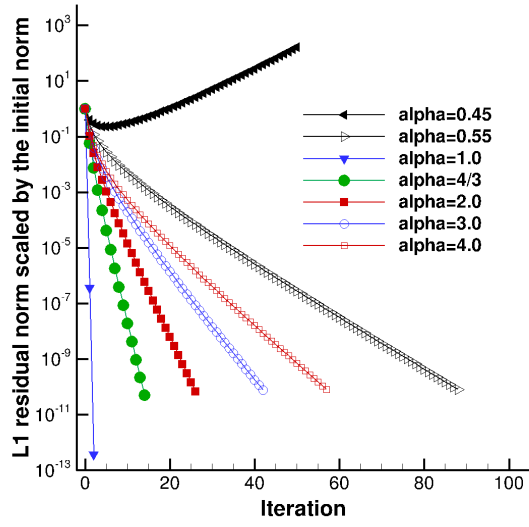
$$f = 16000001\nu\pi^2 \sin(\pi x) \sin(4000\pi y). \quad (4.2)$$

The exact solution is given by

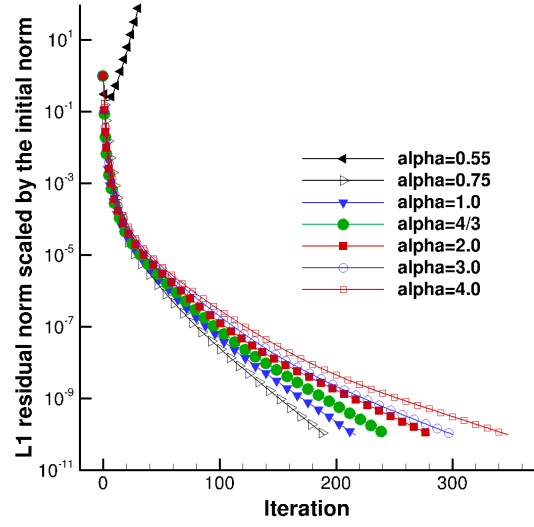
$$u(x, y) = \sin(\pi x) \sin(4000\pi y). \quad (4.3)$$

Again, convergence results are shown for the high-aspect-ratio 64×64 quadrilateral and triangular grids. The grid has uniform spacing in each coordinate direction with $R = 1000$.

Convergence histories are shown in Figure 11. As predicted by the analysis, the solver slows down for larger values of α for both quadrilateral and triangular grids. Moreover, again in good agreement with the analysis,

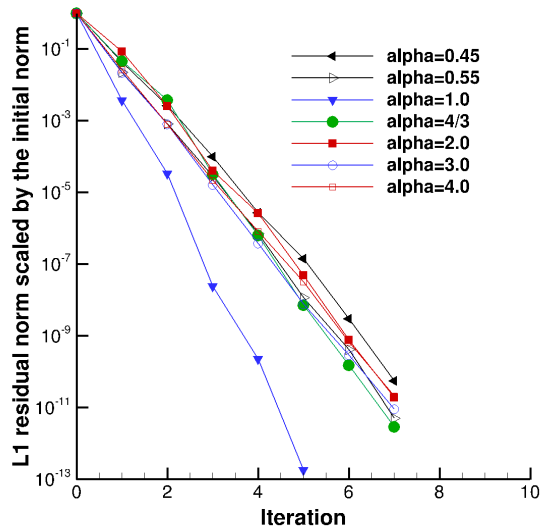


(a) 64×64 quadrilateral grid.

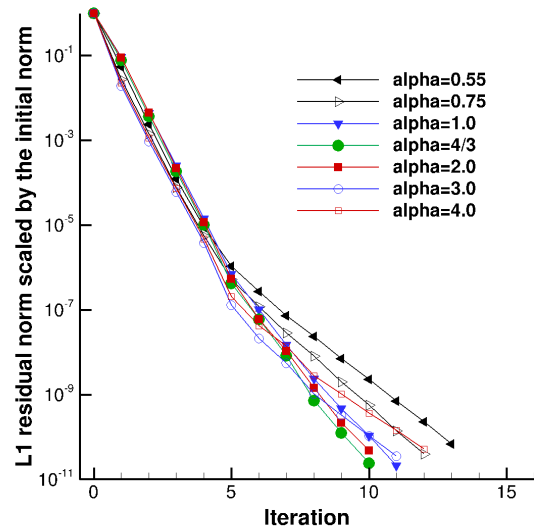


(b) 64×64 triangular grid.

Figure 11: Convergence histories of implicit defect-correction solver for a high-aspect-ratio grid with $R = h_x/h_y = 1000$. Symbols are displayed at every four iterations in (b).



(a) 64×64 quadrilateral grid.



(b) 64×64 triangular grid.

Figure 12: Convergence histories of JFNK-GCR on a high-aspect-ratio grid with $R = h_x/h_y = 1000$.

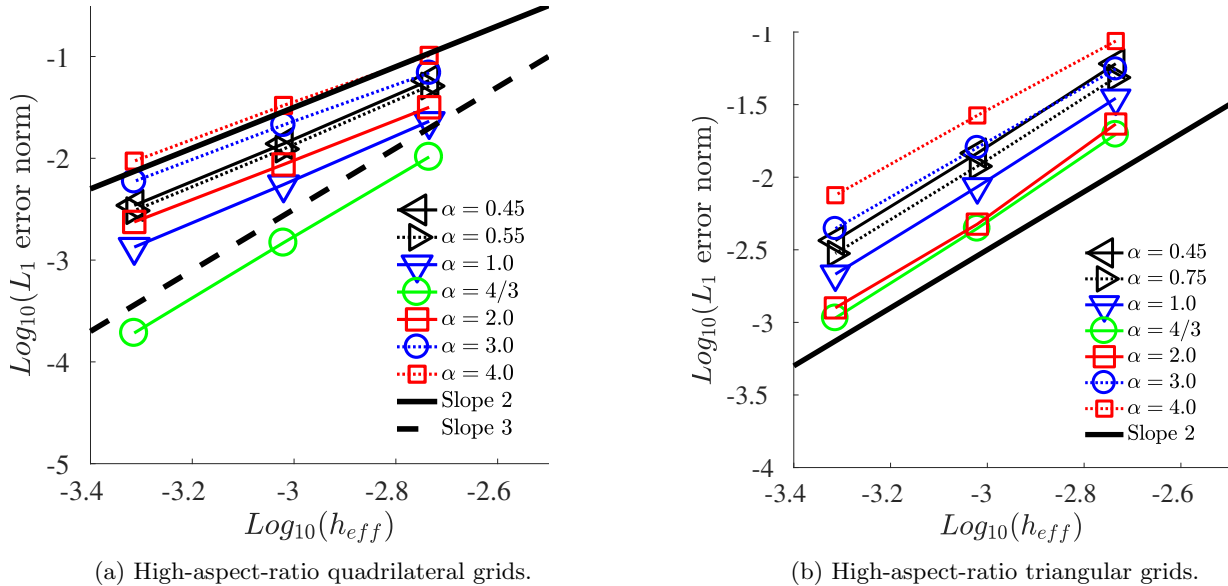


Figure 13: Error convergence results obtained by the JFNK-GCR solver on high-aspect-ratio grids with $R = h_x/h_y = 1000$.

the solver diverges for $\alpha < 0.5$ on the quadrilateral grid and for $\alpha < 0.6$ on the triangular grid. Observe, in particular, that the solver slows down significantly on the high-aspect-ratio triangular grid.

Results obtained by the JFNK-GCR solver are shown in Figure 12. As in the isotropic case, the solver converges very rapidly for all cases; it is quite powerful especially for the triangular-grid case. It demonstrates that the implicit solver can serve as an effective preconditioner for the JFNK-GCR solver even on highly stretched viscous-type grids.

Figure 13 shows the error convergence results. On quadrilateral grids, again, $\alpha = 4/3$ gives third-order accuracy while others yield second-order accuracy as shown in Figure 13(a). For triangular grids, $\alpha = 4/3$ gives the lowest level of errors, similar to $\alpha = 4.0$. The results indicate that the damping term has a significant impact on accuracy for highly-skewed grids.

4.1.3 Irregular High-Aspect-Ratio Grid

To investigate the effect of mesh irregularity and increased skewness, we consider an irregular high-aspect-ratio grid. The grid is generated from the high-aspect-ratio grid used in the previous section by randomly perturbing the nodal coordinates (See Figure 7(c)). Note that even a small nodal perturbation has large impact on the skewness of the triangular grid: the L_1 norm of the skewness measure $\hat{\mathbf{e}}_{jk} \cdot \hat{\mathbf{n}}_{jk}$ is 0.0326 of the perturbed grid, which is an order of magnitude worse than 0.336 on the unperturbed grid. Results are shown in Figure 14. Comparing Figure 14(a) with Figure 11, and Figure 14(b) with Figure 12(b), we see very similar convergence behaviors between perturbed and unperturbed grids. Therefore, mesh irregularities and high skewness have very little effects on iterative convergence. Error convergence results in Figure 14(c) indicate that $\alpha = 4/3$ gives the lowest level of errors, confirming superior accuracy previously reported in Refs.[4, 14]. Also, the JFNK-GCR solver converges for all values of α , including $\alpha = 0.55$ for which the implicit solver diverges, as shown in Figure 17(b).

4.2 Navier-Stokes Equations

To investigate performance of implicit solvers for more practical viscous-flow cases, we consider the compressible Navier-Stokes equations non-dimensionalized by the free stream density, speed of sound, and dynamic pressure. The discretization is the node-centered edge-based method. The inviscid and viscous fluxes are computed by the Roe flux [37] and the alpha-damping flux (via the gradient formula) as described in Ref.[5], respectively. LSQ gradients are computed by an unweighted linear fit. The solutions at a boundary node is determined by solving a residual equation. The residual at a boundary node is closed by a second-order flux quadrature [1]. At each quadrature points, which are boundary nodes, the numerical flux is computed with a

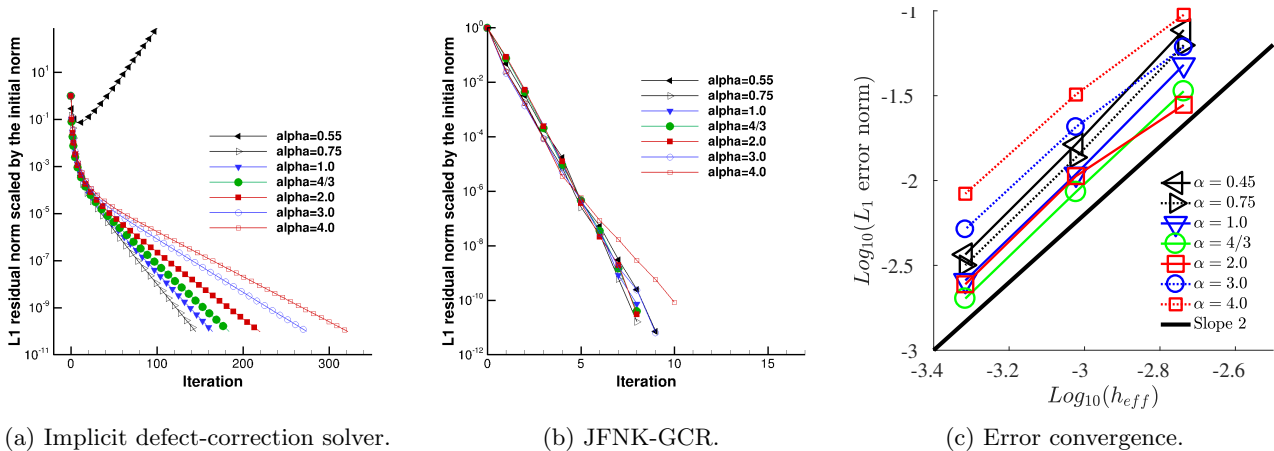


Figure 14: Convergence histories for 64×64 irregular high-aspect-ratio grids with $R = h_x/h_y = 1000$. Symbols are displayed at every four iterations in (a).

current solution as the left state (interior state) and a ghost state specified by a physical boundary condition as the right state.

The implicit solver uses a Jacobian matrix constructed by exactly differentiating the residual with all LSQ gradients ignored, i.e., based on the damping-term-only flux. The linear relaxation is performed by a multi-color Gauss-Seidel method until the linear residual is reduced by half with the maximum of 500. The implicit solver is considered as converged when the L_1 norm of the residual is reduced by ten orders of magnitude or reaches $1.0\text{E}-14$ for all equations. For the JFNK-GCR solver, the tolerance is set to be 0.1 for the preconditioner, and 0.01 for the GCR solver with the maximum number of projections of 10 as a default.

4.2.1 Viscous Shock Problem

First, we consider a viscous shock problem to study the effects of α on accuracy. For the upstream condition, $M_\infty = 3.5$, $Pr = 3/4$, $\gamma = 1.4$, $Re_\infty = 25$, and $T_\infty = 400$ [k], an exact shock-structure solution can be obtained by numerically solving a pair of ordinary differential equations for the velocity and the temperature [38]. The program used to generate the exact solution in this study can be downloaded at <http://www.cfdbooks.com/cfdcodes.html>. A series of four randomly-triangulated grids have been generated with 192, 768, 3072, and 12288 nodes. See Figure 15(a) for the coarsest grid, and the exact x -velocity contours. All results have been obtained by the JFNK-GCR solver with $\alpha = 0.25, 0.75, 1.0, 4/3$, and 2.0. Note that the implicit solver diverges for $\alpha = 0.25$, but the JFNK-GCR solver converges as we will discuss in the next section. Error convergence results for the pressure are given in Figure 15(b); results are very similar for other variables, and therefore not shown. The effective mesh spacing is, again, defined as the L_1 norm of the square root of control volumes around nodes. Second-order order convergence is observed for all values of α , and the error levels are very similar except $\alpha = 2.0$ and 0.25, which result in larger errors. These results indicate that the value of α should not be too far from 1; $\alpha \in [0.75, 4/3]$ yields very similar levels of errors. Note that the special high-order property of $\alpha = 4/3$ for diffusion (Laplacian) is not observed even on Cartesian grids because of the nonlinearity and non-Laplacian nature of the viscous terms, and also of effects of the inviscid terms.

4.2.2 Laminar Flow over a Flat Plate

The implicit defect-correction solver has been tested for a laminar flow over a flat plate at zero incidence with the free stream condition: $M_\infty = 0.15$, $Pr = 3/4$, $\gamma = 1.4$, $Re_\infty = 10^4/(\text{unit grid length})$, and $T_\infty = 300$ [K]. The domain is taken to be a square and the right half of the bottom boundary is taken as a flat plate. The length of the flat plate is 2.0 in the grid, and the Reynolds number based on the flat plate length is, therefore, 2×10^4 . The domain is randomly triangulated with 137×97 nodes as shown in Figure 16. At the inflow and top boundaries, the ghost state is set to be a free stream condition. At the outflow boundary, the ghost state is a copy of the interior state except that the pressure is fixed by a free stream value. At the viscous wall, the density is copied from the interior state, the velocity is reflected (i.e., the interior velocity with a negative sign), and the temperature is set to be a free stream value [39].

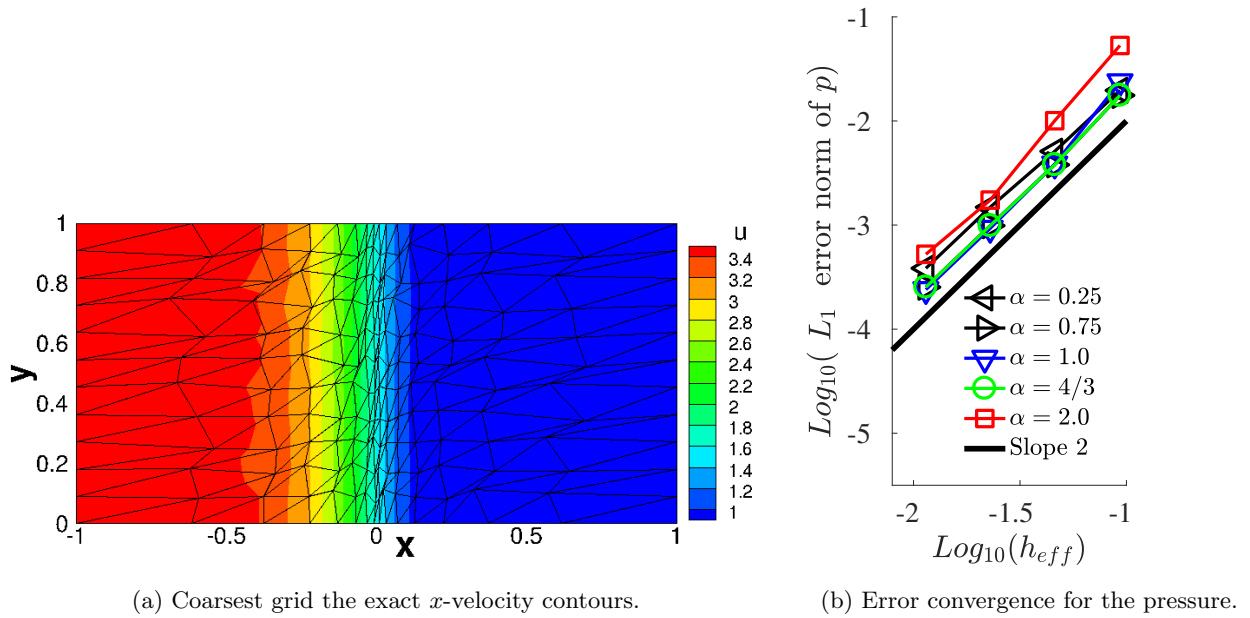


Figure 15: Coarsest grid and error convergence for the pressure in the viscous shock problem.

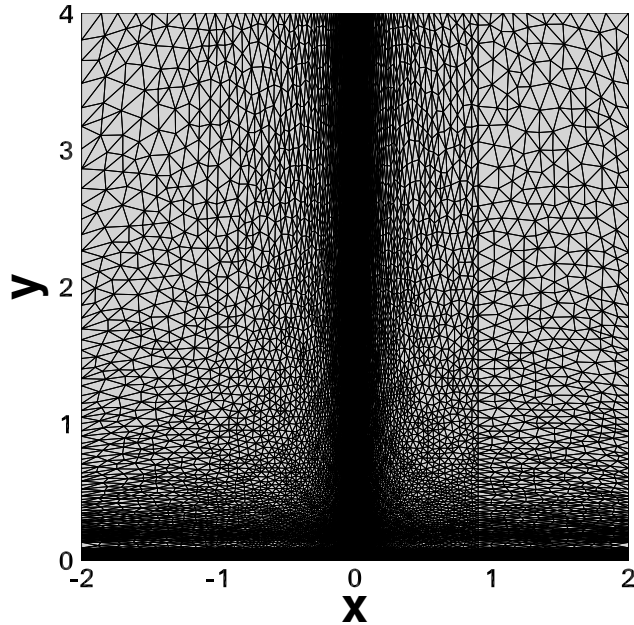


Figure 16: Irregular triangular grid for the flat-plate problem. A flat plate has a length 2.0, and it is located at the bottom of the domain starting at $x = 0$ and ending at $x = 2.0$. A vertical grid line has been introduced precisely at $x = 0.9$ to sample the solution for comparison.

Convergence histories are shown in Figure 17. As can be seen in Figure 17(a), the value of α has a very minor impact on the iterative convergence, seemingly due to a large impact of the inviscid terms, except that the solver diverges for $\alpha = 0.55$ just like the diffusion equation case on irregular high-aspect-ratio triangular grids (see Figures 11(b) and 14(a)). It indicates an important implication that a lack of viscous damping can lead to instability even for convection-dominated flows. As expected, however, the JFNK-GCR solver converges

for all values of α , even for $\alpha = 0.55$, demonstrating its robustness for a wider range of α . For the solutions obtained by the JFNK-GCR solver, velocity profiles sampled along a vertical line at $x = 0.9$ are plotted in Figure 18. The profiles are very similar, and therefore they are not greatly influenced by the choice of α .

To investigate the efficiency of the JFNK-GCR solver, we performed the same computation for $\alpha = 4/3$ with various numbers of GCR projections: JFNK-GCR(n), where n is the number of GCR projections, $n = 0, 1, 4, 8, 16, 32$. JFNK-GCR(0) corresponds to the implicit defect-correction solver. Results are shown in Figure 19. As can be seen, the JFNK-GCR(n) solver with $n > 0$ converged faster in CPU time than JFNK-GCR(0). Further details of the JFNK-GCR(n) solver are shown in Figure 20. Figure 20(a) shows the actual GCR projections performed to reduce the GCR residual by two orders of magnitude. In most cases, the tolerance is not met within the specified number of projections. For $n = 32$, the tolerance is met before it reaches the maximum 32. Figure 20(b) shows the number of linear relaxations in the variable-preconditioner step. It is noted that $n = 1$ took less numbers of linear relaxations than $n = 0$, and this explains (with a less number of iterations) a significant speed-up in CPU time as observed in Figure 19(b). These results indicate that even a very small number of GCR projections can yield robust and efficient computations over the implicit defect-correction solver. In Ref.[32], $n = 4$ is demonstrated to provide robust and efficient three-dimensional computations for practical turbulent-flow problems.

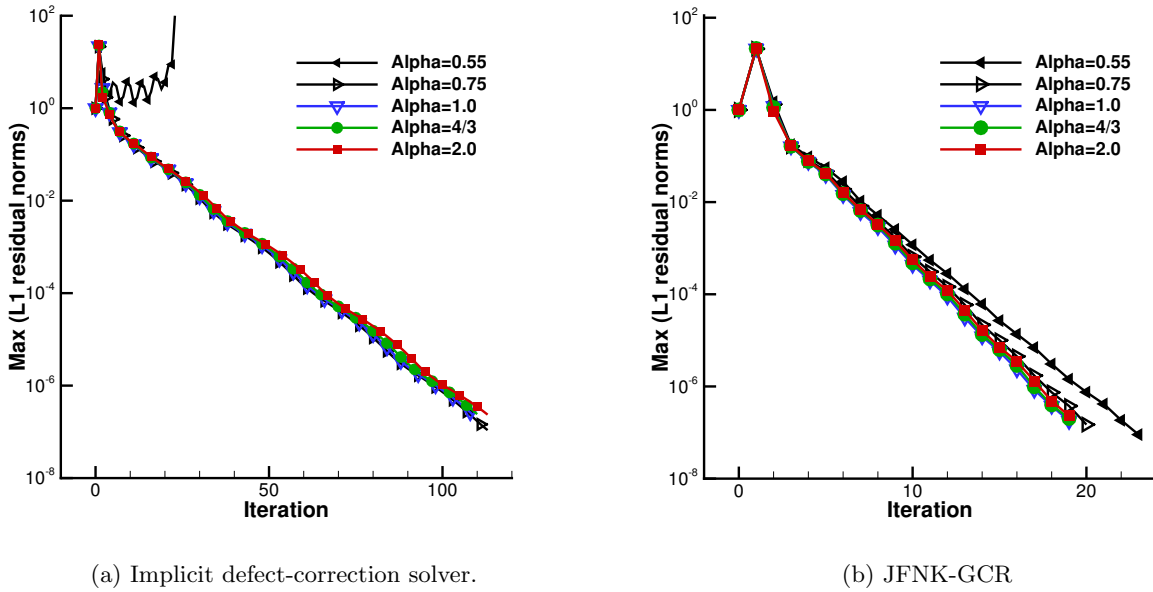
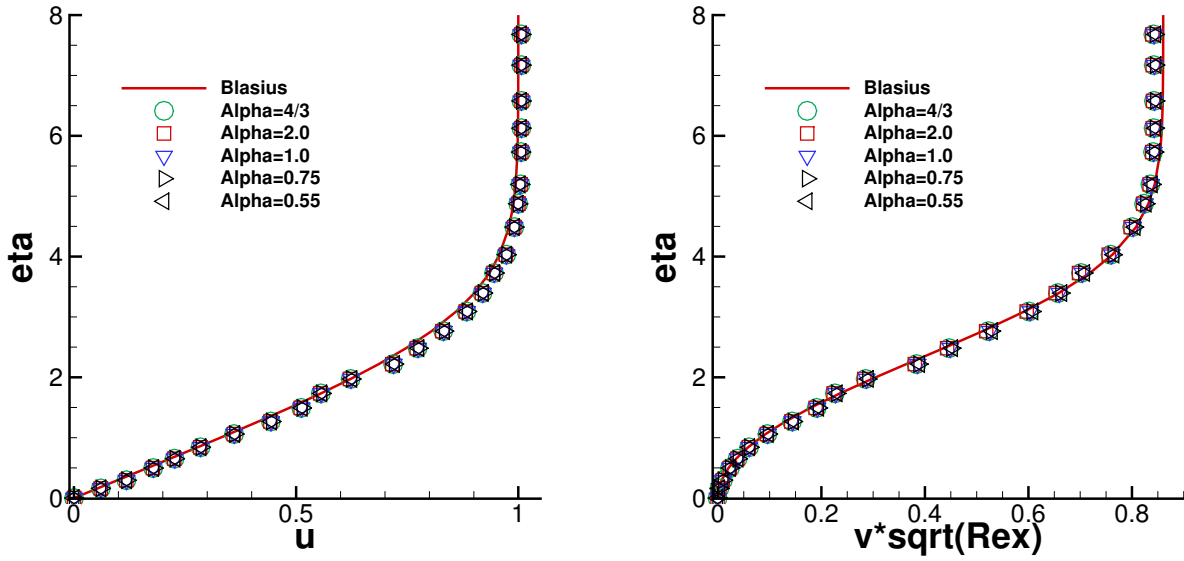


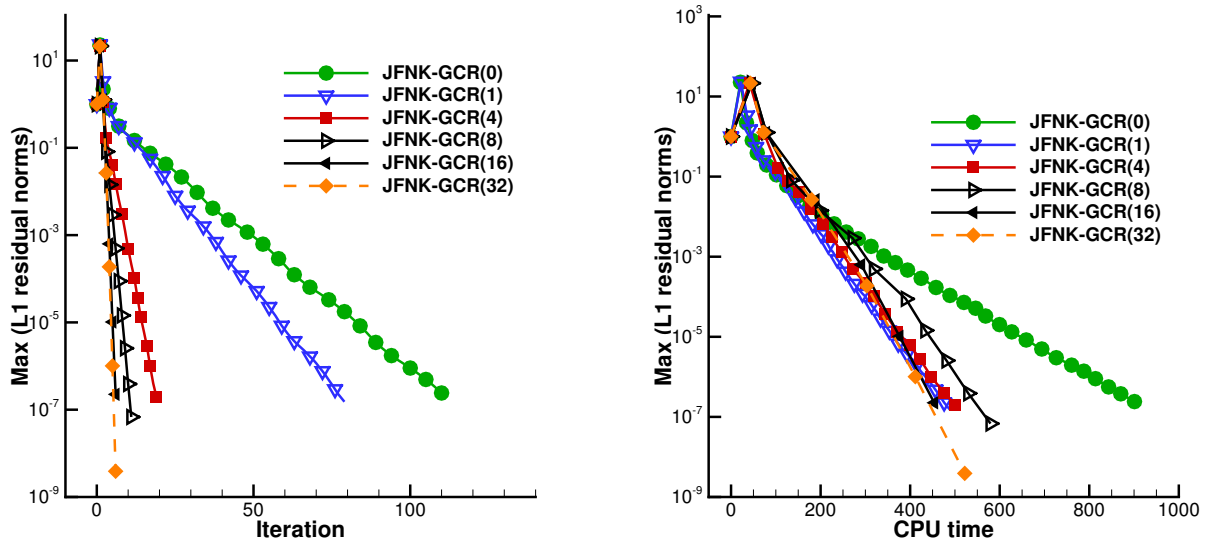
Figure 17: Convergence histories for the flat plate case.



(a) X-velocity profile.

(b) Y-velocity profile.

Figure 18: Solution profiles at $x = 0.9$. Values are plotted at every other node along the line $x = 0.9$. The vertical axis is taken as the boundary-layer coordinate, $\eta = y\sqrt{Re_x}/x$, where Re_x is the Reynolds number based on the distance along the plate from the leading edge, which has been used also to scale the transverse velocity.



(a) Iteration.

(b) CPU time (sec)

Figure 19: Convergence histories of the JFNK-GCR solver with various numbers of GCR projections ($\alpha = 4/3$).

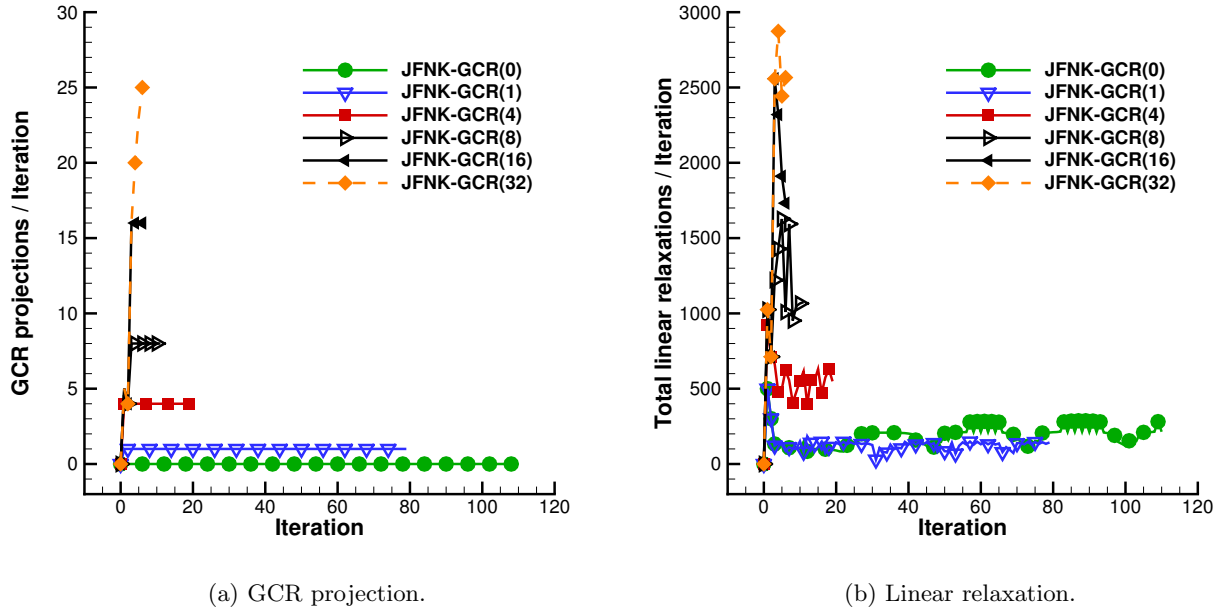


Figure 20: GCR projections and linear relaxations per iteration ($\alpha = 4/3$).

5 Concluding Remarks

A Fourier analysis was performed to investigate effects of a damping parameter α in a damped viscous scheme on iterative convergence of an implicit defect-correction solver on quadrilateral and triangular grids. For regular quadrilateral grids, the analysis shows that the best convergence is achieved for $\alpha = 1$, the solver slows down for larger values of α , and diverges for $\alpha < 0.5$. Also, it has been shown that $\alpha = 4/3$ provides third-order accuracy on isotropic as well as high-aspect-ratio quadrilateral grids for the node-centered edge-based method. A similar convergence behavior was predicted for regular triangular grids; the implicit solver diverges for $\alpha < 0.6$. These findings have been confirmed by numerical experiments. For irregular high-aspect-ratio grids, a similar convergence behavior has been observed, and $\alpha = 4/3$ gives the lowest level of errors. The implicit solver has been shown to serve as an effective preconditioner for a Jacobian-Free Newton-Krylov solver based on the GCR method. The Newton-Krylov solver has been shown to converge in all cases considered, including those for which the implicit solver diverges. For diffusion problems, the Jacobian-Free Newton-Krylov solver with $\alpha = 4/3$ is recommended for very accurate, efficient, and robust computations. For the Navier-Stokes equations, the implicit solver does not show large variation among α for a flat plate test case, but it has been found to diverge for $\alpha = 0.55$. The Jacobian-Free Newton-Krylov solver, however, converges for all values of α considered, and converges faster than the implicit solver in CPU time by a factor of 4, at least. The study indicates that the damping coefficient $\alpha = 4/3$ or close to 1 and the GCR-based Jacobian-Free Newton-Krylov solver with the implicit defect-correction solver used as a variable preconditioner can be a robust and accurate combination for practical viscous flow problems.

Acknowledgments

The first author gratefully acknowledges support from Software CRADLE.

References

- [1] Nishikawa, H., Diskin, B., and Thomas, J. L., “Development and Application of Agglomerated Multigrid Methods for Complex Geometries,” *Proc. of 40th AIAA Fluid Dynamics Conference and Exhibit*, AIAA Paper 2010-4731, Chicago, 2010.

- [2] Thomas, J. L., Diskin, B., and Nishikawa, H., “A Critical Study Agglomerated Multigrid Methods for Diffusion on Highly-Stretched Grids,” *Comput. Fluids*, Vol. 40, No. 1, February 2010, pp. 82–93.
- [3] Nishikawa, H., “Beyond Interface Gradient: A General Principle for Constructing Diffusion Schemes,” *Proc. of 40th AIAA Fluid Dynamics Conference and Exhibit*, AIAA Paper 2010-5093, Chicago, 2010.
- [4] Nishikawa, H., “Robust and Accurate Viscous Discretization via Upwind Scheme - I: Basic Principle,” *Comput. Fluids*, Vol. 49, No. 1, October 2011, pp. 62–86.
- [5] Nishikawa, H., “Two Ways to Extend Diffusion Schemes to Navier-Stokes Schemes: Gradient Formula or Upwinding,” *20th AIAA Computational Fluid Dynamics Conference*, AIAA Paper 2011-3044, Honolulu, Hawaii, 2011.
- [6] Haselbacher, A., McGuirk, J. J., and Page, G. J., “Finite Volume Discretization Aspects for Viscous Flows on Mixed Unstructured Grids,” *AIAA J.*, Vol. 37, No. 2, 1999, pp. 177–184.
- [7] Pincock, B. and Katz, A., “High-Order Flux Correction for Viscous Flows on Arbitrary Unstructured Grids,” *J. Sci. Comput.*, Vol. 61, 2014, pp. 454–476.
- [8] Venkatakrishnan, V. and Mavriplis, D. J., “A Unified Multigrid Solver for the Navier-Stokes Equations on Mixed Element Meshes,” *ICASE Report 95-53*, 1995.
- [9] Nishikawa, H., “On Viscous Scheme for Cell-Centered Method,” Unpublished, http://www.cfdnotes.com/cfdnotes_on_cell_centred_viscous_scheme2015.pdf, November, 2015.
- [10] Muppidi, S. and Mahesh, K., “Direct Numerical Simulation of Passive Scalar Transport in Transverse Jets,” *J. Fluid Mech.*, Vol. 598, 2008, pp. 335–360.
- [11] Abgrall, R., De Santis, D., and Ricchiuto, M., “High-Order Preserving Residual Distribution Schemes for Advection-Diffusion Scalar Problems on Arbitrary Grids,” *SIAM J. Sci. Comput.*, Vol. 36, No. 3, 2014, pp. A955–A983.
- [12] Arnold, D. N., “An Interior Penalty Finite Element Method with Discontinuous Elements,” *SIAM J. Numer. Anal.*, Vol. 19, No. 4, 1982, pp. 742–760.
- [13] Cary, A. W., Dorgan, A. J., and Mani, M., “Towards Accurate Flow Predictions Using Unstructured Meshes,” *Proc. of 39th AIAA Fluid Dynamics Conference*, AIAA Paper 2009-3650, San Antonio, 2009.
- [14] Jalali, A., Sharbatdar, M., and Ollivier-Gooch, C., “Accuracy Analysis of Unstructured Finite Volume Discretization Schemes for Diffusive Fluxes,” *Comput. Fluids*, Vol. 101, September 2014, pp. 220–232.
- [15] Abbas, Q. and Nordstrom, J., “Weak versus Strong No-Slip Boundary Conditions for The Navier-Stokes Equations,” *Eng. Appl. Comp. Fluid.*, Vol. 4, No. 1, 2010, pp. 29–38.
- [16] Nordstrom, J., Eriksson, S., and Eliasson, P., “Weak and strong wall boundary procedures and convergence to steady-state of the NavierStokes equations,” *J. Comput. Phys.*, Vol. 231, 2012, pp. 4867–4884.
- [17] Nakashima, Y., Watanabe, N., and Nishikawa, H., “Development of an Effective Implicit Solver for General-Purpose Unstructured CFD Software,” *The 28th Computational Fluid Dynamics Symposium*, C08-1, Tokyo, Japan, 2014.
- [18] Sejkan, C. B. and Ollivier-Gooch, C. F., “Improving finite-volume diffusive fluxes through better reconstruction,” *Comput. Fluids*, Vol. 139, 2016, pp. 216–232.
- [19] Jalali, A. and Ollivier-Gooch, C., “Higher-order unstructured finite volume RANS solution of turbulent compressible flows,” *Comput. Fluids*, Vol. 143, 2017, pp. 32–47.
- [20] Nishikawa, H., “Accuracy-Preserving Boundary Flux Quadrature for Finite-Volume Discretization on Unstructured Grids,” *J. Comput. Phys.*, Vol. 281, 2015, pp. 518–555.
- [21] Biedron, R. T., Carlson, J.-R., Derlaga, J. M., Gnoffo, P. A., Hammond, D. P., Jones, W. T., Kleb, B., Lee-Rausch, E. M., Nielsen, E. J., Park, M. A., Rumsey, C. L., Thomas, J. L., and Wood, W. A., “FUN3D Manual: 12.9,” *NASA-TM-2016-219012*, February 2016.

- [22] Kroll, N., Abu-Zurayk, M., Dimitrov, D., Franz, T., Führer, T., Gerhold, T., Görtz, S., Heinrich, R., Ilic, C., Jepsen, J., Jägersküpper, J., Kruse, M., Krumbein, A., Langer, S., Liu, D., Liepelt, R., Reimer, L., Ritter, M., Schwöppe, A., Scherer, J., Spiering, F., Thormann, R., Togiti, V., Vollmer, D., and Wendisch, J.-H., “DLR Project Digital-X: Towards Virtual Aircraft Design and Flight Testing Based on High-Fidelity Methods,” *CEAS Aeronautical Journal*, Vol. 7, No. 1, March 2016, pp. 3–27.
- [23] Mavriplis, D. J. and Long, M., “NSU3D Results for the Fourth AIAA Drag Prediction Workshop,” AIAA Paper 2010-4363, 2010.
- [24] Luo, H., Baum, J. D., and Löhner, R., “High-Reynolds Number Viscous Flow Computations using an Unstructured-Grid Method,” *Proc. of 42nd AIAA Aerospace Sciences Meeting*, AIAA Paper 2004-1103, Reno, Nevada, 2004.
- [25] Kozubskaya, T., Abalakin, I., Dervieux, A., and Ouvrard, H., “Accuracy Improvement for Finite-Volume Vertex-Centered Schemes Solving Aeroacoustics Problems on Unstructured Meshes,” *Proc. of 16th AIAA/CEAS Aeroacoustics Conference*, AIAA Paper 2010-3933, 2010.
- [26] Haselbacher, A. and Blazek, J., “Accurate and Efficient Discretization of Navier-Stokes Equations on Mixed Grids,” *AIAA J.*, Vol. 38, No. 11, 2000, pp. 2094–2102.
- [27] Masatsuka, K., “I do like CFD, VOL.1, Second Edition, Version 2.4,” <http://www.cfdbooks.com>, 2017.
- [28] Svärd and J. Nordström, M., “Stability of Finite Volume Approximations for the Laplacian Operator on Quadrilateral and Triangular Grids,” *Appl. Numer. Math.*, Vol. 51, 2004, pp. 101–125.
- [29] Diskin, B. and Thomas, J. L., “Accuracy Analysis for Mixed-Element Finite-Volume Discretization Schemes,” *NIA Report No. 2007-08*, 2007.
- [30] Eisenstat, S. C., Elman, H. C., and Schultz, M. H., “Variational Iterative Methods for Nonsymmetric Systems of Linear Equations,” *SIAM J. Numer. Anal.*, Vol. 20, No. 2, 1983, pp. 345–357.
- [31] Axelsson, O. and Vassilevski, P. S., “A Black Box Generalized Conjugate Gradient Solver with Inner Iterations and Variable-Step Preconditioning,” *SIAM J. Matrix. Anal. A.*, Vol. 12, No. 4, 1991, pp. 625–644.
- [32] Pandya, M. J., Diskin, B., Thomas, J. L., and Frink, N. T., “Improved Convergence and Robustness of USM3D Solutions on Mixed Element Grids,” *AIAA J.*, Vol. 54, No. 9, September 2016, pp. 2589–2610.
- [33] Abe, K. and Liang Zhang, S., “A Variable Preconditioning Using the SOR Method for GCR-Like Methods,” *Int. J. Numer. Anal. Model.*, Vol. 2, No. 2, 2005, pp. 147–161.
- [34] Nishikawa, H., Diskin, B., Thomas, J. L., and Hammond, D. H., “Recent Advances in Agglomerated Multigrid,” *51st AIAA Aerospace Sciences Meeting*, AIAA Paper 2013-863, Grapevine, Texas, 2013.
- [35] Diskin, B. and Thomas, J. T., “Convergence of defect-correction and multigrid iterations for inviscid flows,” *Proc. of 20th AIAA Computational Fluid Dynamics Conference*, AIAA Paper 2011-3235, Honolulu, Hawaii, 2011.
- [36] Trottenberg, U., Oosterlee, C. W., and Schüller, A., *Multigrid*, Academic Press, 2000.
- [37] Roe, P. L., “Approximate Riemann Solvers, Parameter Vectors, and Difference Schemes,” *J. Comput. Phys.*, Vol. 43, 1981, pp. 357–372.
- [38] Xu, K., “A Gas-Kinetic BGK Scheme for the Navier-Stokes Equations and Its Connection with Artificial Dissipation and Godunov Method,” *J. Comput. Phys.*, Vol. 171, 2001, pp. 289–335.
- [39] Mengaldo, G., Grazia, D. D., Witherden, F., Farrington, A., Vincent, P., Sherwin, S., and Peiro, J., “A Guide to the Implementation of Boundary Conditions in Compact High-Order Methods for Compressible Aerodynamics,” *Proc. of 7th AIAA Theoretical Fluid Mechanics Conference, AIAA Aviation and Aeronautics Forum and Exposition 2014*, AIAA Paper 2014-2923, Atlanta, GA, 2014.